Article

Interface-controlled uniaxial in-plane ferroelectricity in $Hf_{0.5}Zr_{0.5}O_2$(100) epitaxial thin films

Kai Liu[1,11], Feng Jin[1,11], Tianyuan Zhu[2,3,11], Jie Fang[1,11], Xingchang Zhang[4], Erhao Peng[5], Kuan Liu[1], Qiming Lv[1], Kunjie Dai[1], Yajun Tao[5], Jingdi Lu[1], Haoliang Huang[6], Jiachen Li[7], Shouzhe Dong[8], Shengchun Shen[7], Yuewei Yin[7], Houbing Huang[8], Zhenlin Luo[5]✉, Chao Ma[4]✉, Shi Liu[2,3]✉, Lingfei Wang[1]✉ & Wenbin Wu[1,9,10]✉

Hafnium oxide-based ferroelectric thin films are widely recognized as a CMOS-compatible and highly scalable material platform for next-generation non-volatile memory and logic devices. While out-of-plane ferroelectricity in hafnium oxide films has been intensively investigated and utilized in devices, purely in-plane ferroelectricity of hafnium oxides remains unexplored. In this work, we demonstrate a reversible structural modulation of the orthorhombic phase $Hf_{0.5}Zr_{0.5}O_2$ films between (111)-oriented [HZO(111)$_O$] multi-domain and (100)-oriented [HZO(100)$_O$] single-domain configurations by altering perovskite oxide buffer layers. Unlike conventional out-of-plane polarized HZO(111)$_O$ films, the HZO(100)$_O$ films exhibit uniaxial in-plane ferroelectric polarization, sustained even at a thickness of 1.0 nm. Furthermore, the in-plane ferroelectric switching achieves an ultralow coercivity of ~0.5 MV/cm. The HZO(100)$_O$ phase is stabilized by a staggered interfacial reconstruction, driven by the delicate interplays between symmetry mismatch and surface energy. These findings pave the way for innovative device designs and strategies for modulating the functionalities of hafnium oxide-based ferroelectrics.

Ferroelectric (FE) thin film has been recognized as a key component for developing nonvolatile memory devices, mainly due to their highly tunable and electrically switchable FE polarization[1–3]. Although the current mainstream FE memory architectures, including FE random-access memory, FE tunnel junctions, and FE field-effect transistors, are all developed based on FE thin films with out-of-plane polarization[4], the FE thin films with tilted or purely in-plane polarizations have also attracted burgeoning research interests during the past decades[5–9]. The in-plane FE polarization is strongly coupled with the ferroelastic strain, electrostatic potential, octahedral rotation, and mobile carriers in the heteroepitaxial heterostructures, which stabilizes intriguing physical phenomena such as polar vortex[7], self-organized "superdomains"[8], and hybrid improper ferroelectricity[9]. Moreover, the in-plane polarization switching can effectively deplete or accumulate mobile carriers at the

[1]Hefei National Research Center for Physical Sciences at the Microscale, University of Science and Technology of China, Hefei, China. [2]Department of Physics, School of Science, Westlake University, Hangzhou, China. [3]Institute of Natural Sciences, Westlake Institute for Advanced Study, Hangzhou, China. [4]College of Materials Science and Engineering, Hunan University, Changsha, China. [5]National Synchrotron Radiation Laboratory, University of Science and Technology of China, Hefei, China. [6]Quantum Science Center of Guangdong-Hong Kong-Macao Greater Bay Area, Shenzhen, China. [7]Department of Physics, University of Science and Technology of China, Hefei, China. [8]Advanced Research Institute of Multidisciplinary Science, Beijing Institute of Technology, Beijing, China. [9]Institutes of Physical Science and Information Technology, Anhui University, Hefei, China. [10]Collaborative Innovation Center of Advanced Microstructures, Nanjing University, Nanjing, China. [11]These authors contributed equally: Kai Liu, Feng Jin, Tianyuan Zhu, Jie Fang. ✉e-mail: zlluo@ustc.edu.cn; cma@hnu.edu.cn; liushi@westlake.edu.cn; wanglf@ustc.edu.cn; wuwb@ustc.edu.cn

charge domain walls and heterointerfaces, which offers new device designs with non-volatile memory and logic functionalities[7–12]. According to these exciting progresses, developing suitable methods to modulate the FE film polarization directions (out-of-plane or in-plane) could be essential for the future advancements of FE thin-film-based research, in both fundamental and device application aspects.

HfO$_2$-based thin films have been recognized as one of the most promising ferroelectrics due to their robust FE polarization for thickness down-scaling and CMOS-compatibility[13–15]. Recent advancements in lowering coercive fields (E_C) of HfO$_2$-based thin films further pave the way for cost-effective memory devices[16,17]. Note that most of the currently reported FE hafnium oxide films and related devices utilize out-of-plane polarization only[18]. Harnessing the FE polarization direction and achieving purely in-plane polarization, if realized in HfO$_2$-based ferroelectrics, could further leverage their appealing features and expand their application potential for innovative nanoelectronics. However, most HfO$_2$-based FE films are polycrystalline with random polarization directions, which complicates the modulation and evolution of the FE film polarization components[19,20].

Compared with the polycrystalline counterparts, HfO$_2$-based FE films epitaxially grown on ABO$_3$ perovskite oxides exhibit much more uniform structural domain configuration and growth orientation[21–23]. Although these films are grown in a domain-matching epitaxial growth mode[24], epitaxial strain has considerable impacts on the volume ratio and spatial distribution of polar/non-polar phases in epitaxial Hf$_{0.5}$Zr$_{0.5}$O$_2$ (HZO) films[25,26]. Recent literature further highlights the critical role of HZO/ABO$_3$ heterointerface structure in stabilizing the structural phase and even modulating the FE properties[27–29]. Accordingly, clarifying and harnessing the interfacial coupling mechanism between HZO and ABO$_3$ perovskite lattices could further enhance the tunability of FE properties and even achieve purely in-plane ferroelectricity in the HZO films.

In this work, by harnessing the interfacial coupling between HZO and ABO$_3$ perovskite lattices, we can flexibly switch the growth orientations of HZO films. Specifically, the HZO film grown on La$_{0.67}$Sr$_{0.33}$MnO$_3$(110) [LSMO(110)] surface shows typical (111)-oriented orthorhombic (O) multi-domains, while the film grown on SrTiO$_3$(110) [STO(110)] displays an unconventional (100)-oriented O phase [HZO(100)$_O$]. Comprehensive FE characterizations on these HZO(100)$_O$ films demonstrate an uniaxially-polarized in-plane ferroelectricity, which is rarely observed in HfO$_2$-based ferroelectrics. The [001]$_O$-oriented FE polarization can persist in the HZO(100)$_O$ film even down to 1 nm thick. Atomic-scale structural characterizations and density functional theory (DFT) calculations further revealed that this uniaxial in-plane ferroelectricity is stabilized by a "stagger-like" reconstruction at the HZO(100)$_O$/STO(110) interface, triggered by the subtle balance between symmetry mismatch and surface energy. Our work showcases an effective modulation of the FE polarization orientation of HfO$_2$-based heterostructures, which is expected to open a novel pathway for exploring innovative FE device designs of non-volatile memory and logic functionalities.

Results

We grew the HZO films on LSMO-buffered STO(110) substrates using pulsed laser deposition (see procedural details in the Method Section). We fixed the thickness of the HZO layer (t_{HZO}) at 10 nm and varied the thickness of the LSMO buffer layer (t_{LSMO}) from 0 to 70 unit cells (u.c., one unit-cell corresponds to ~0.28 nm). Interestingly, the X-ray diffraction (XRD) 2θ-ω linear scans of the HZO/LSMO/STO(110) heterostructures (Fig. 1a) strongly suggest that the structural phase and growth orientation of HZO can be effectively modulated by adjusting t_{LSMO}. For the samples with t_{LSMO} ≥5 u.c., the Bragg reflection of the HZO layer appears at 2θ ~ 30.2°, corresponding to the (111) diffraction of FE O-phase [HZO(111)$_O$, Fig. 1d][25]. The clear Laue fringes around the HZO(111)$_O$ diffraction and sharp rocking curves further attest to the

high epitaxial quality (Supplementary Fig. S1). This HZO(111)$_O$ diffraction peak intensity decays gradually as t_{LSMO} decreases to 3 and 2 u.c. Meanwhile, another diffraction peak emerges at 2θ ~ 34.2°, close to the (100) diffraction of HZO M-phase [HZO(100)$_M$]. For the HZO film grown directly on STO(110) substrate (t_{LSMO} = 0), the 2θ-ω curve only displays a diffraction peak at 2θ ~ 33.7°, which is close to the HZO(100)$_O$ diffraction. Temperature-dependent 2θ-ω curves (Supplementary Fig. S2) further reveal distinct tetragonal (T) to O-phase transitions upon cooling. The HZO/LSMO/STO(110) sample exhibits a clear structure phase transition from T(101) to O(111), consistent with previous reports[30]. By contrast, the HZO/STO(110) sample displays a continuous peak shift only, corresponding to the transition from HZO(001)$_T$ to HZO(100)$_O$, accompanied by a gradual increase of out-of-plane lattice constant.

To identify the nature of LSMO buffer layer-mediated structural modulation, we further introduced multi-layer buffers underneath HZO and characterized the structural evolutions. As shown in Fig. 1b, we first inserted an additional STO layer between the 5 u.c. LSMO layer and the 10 nm HZO layer [HZO/STO/LSMO/STO(110)]. As the thickness of the STO (t_{STO}) layer increases, the HZO(111)$_O$ diffraction peak gradually decays while the HZO(100)$_M$ and HZO(100)$_O$ diffractions emerge in the 2θ-ω linear scan. As t_{STO} increases to 5 u.c., the 2θ-ω linear scan displays HZO(100)$_O$ diffraction only. Second, we further inserted an additional LSMO layer between the HZO and the aforementioned STO(5 u.c.)/LSMO(5 u.c.) bilayer buffer. As the t_{LSMO} becomes thicker, we observed the recovery of HZO(111)$_O$ diffraction (Fig. 1c). These results strongly suggest the pivotal role of the buffer-layer surface [LSMO(110) or STO(110)] in determining the structural phase and growth orientation of the HZO films. In other words, the HZO structural modulation should be interface-mediated.

We now turn to investigate the atomic structure of the HZO/LSMO/STO(110) and HZO/STO(110) heterostructures. Figure 2a shows the high-resolution scanning transmission electron microscopy (STEM) images of the HZO/LSMO(5 u.c.)/STO(110) sample, acquired in high-angle annular dark field (HAADF) mode and viewed along the STO[001] zone axis. Moreover, the HZO region of the HAADF-STEM image displays a multiple-domain configuration. All the domains share the same out-of-plane (111)$_O$ axis but distinct in-plane crystallographic orientations. The fast Fourier transform (FFT) analysis (Fig. 2b) further confirms that the HZO domains are (111)$_O$-oriented O-phase. And the structure model (Fig. 2c) aligns well with the HAADF-STEM image. In sharp contrast, the HAADF-STEM image of the HZO/STO(110) sample (Fig. 2e) displays a distinct atomic structure and epitaxial relationship. To image the atomic structure of the HZO/STO(110) sample, we acquired the STEM image along a specified zone axis: rotating by 45° with respect to the STO[001] axis[31]. Viewed along this axis, the STO(110) region shown in Fig. 2e only displays dim lines while the HZO region displays a uniform atomic contrast, in which the Hf (Zr) atoms self-organize into paired columns. By comparing the FFT pattern and structure model (Fig. 2f, g), we confirmed that the HZO film turns out to be (100)$_O$-oriented O-phase. The distinct atomic arrangements between HZO/LSMO(110) and HZO/STO(110) heterostructures further suggest the essential role of the interface in modulating the HZO structure.

To further reveal the epitaxial relationships and domain configurations of the HZO/LSMO/STO(110) and HZO/STO(110) heterostructures, we conducted pole figure measurements around asymmetrical HZO{111}$_O$ reflections (Fig. 2d, h). For the HZO/LSMO/STO(110) sample, the pole figure of the HZO(111)$_O$ shows 12 {111}$_O$ reflections located at χ ~ 71° (Fig. 2d). These reflections are paired into six sets, each separated by an azimuthal angle φ ~ 60°, indicating the presence of 4 HZO domain variants. The corresponding epitaxial relationships between these 4 HZO domain variants and the LSMO buffer layer are depicted in Fig. 2d: HZO[01-1]$_O$//LSMO[2-2-1], HZO[01-1]$_O$//LSMO[2–21], HZO[01-1]$_O$//LSMO[-22-1], and HZO[01-1]$_O$//LSMO[-221]. Such a 4-variants domain
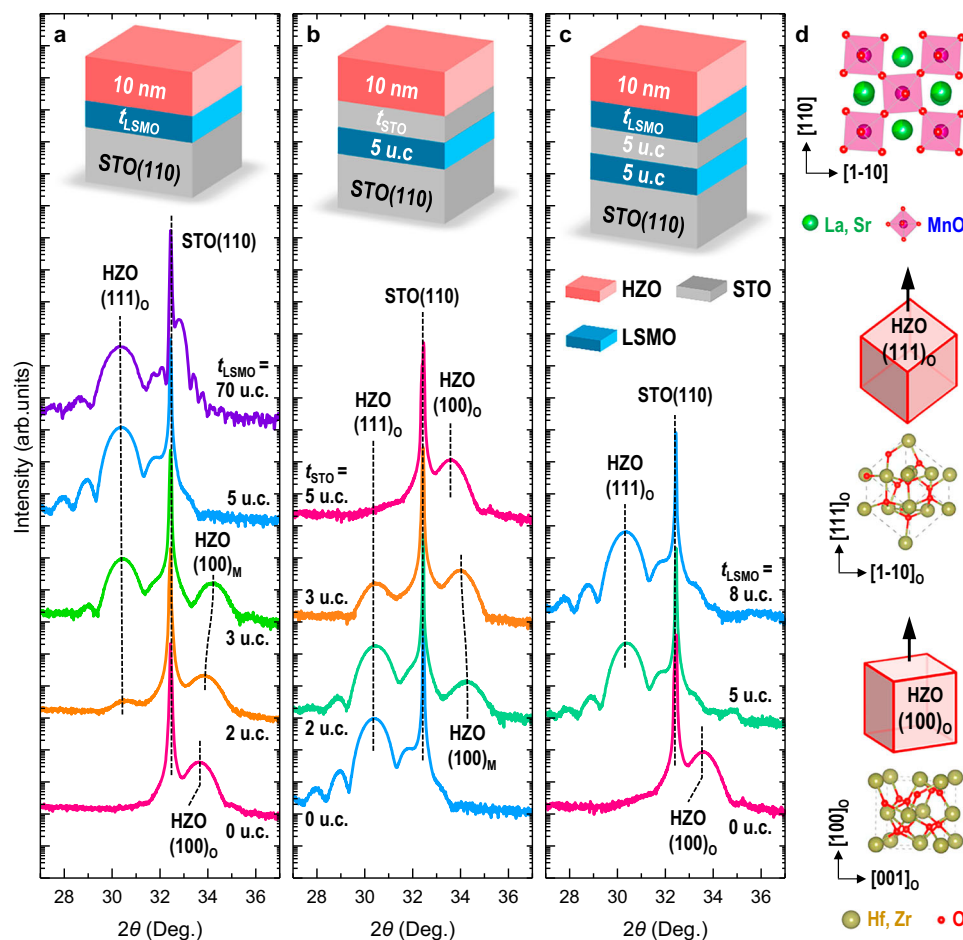
Fig. 1 | Structural evolutions of HZO-based heterostructures on STO(110) substrate. a XRD $2\theta-\omega$ linear scans of HZO films grown on LSMO-buffered STO(110) substrates. The thickness of LSMO buffer layer t_{LSMO} varies from 0 to 70 u.c. **b** XRD $2\theta-\omega$ linear scans of HZO films grown on STO/LSMO bilayer buffered STO(110) substrates. The thickness of STO layer (t_{STO}) varies from 0 to 5 u.c. **c** XRD $2\theta-\omega$ linear scans of HZO films grown on LSMO/STO(5 u.c.)/LSMO(5 u.c.) tri-layer buffered STO(110) substrates. The thickness of the top LSMO buffer layer (t_{LSMO}) varies from 0 to 8 u.c. The (111), (100) diffractions of orthorhombic HZO [HZO(111)$_O$ and HZO(100)$_O$] and the (100) diffractions of monoclinic are marked by dashed lines. The insets are schematic stacking sequences of these HZO-based heterostructures. The thickness of HZO layer (t_{HZO}) is fixed at 10 nm. **d** Schematic illustration of the atomic structure and growth orientations of the LSMO and orthorhombic HZO unit cell.

configuration is stabilized by the interplay between strain-mediated symmetry modulation and the surface energy[22,25,26].

Compared to the HZO/LSMO/STO(110) sample, the HZO/STO(110) sample displays a distinct domain configuration and epitaxial relationship. The pole figure (Fig. 2h) only displays four bright HZO{-111}$_O$ spots near χ ~ 55°, separated by an azimuthal angle φ ~ 90°, demonstrating a four-fold symmetry. In this regard, the epitaxial relationship between HZO(100)$_O$ and STO(110) is much simpler: HZO[011]//STO[1−10] and HZO[01-1]//STO[002] (Fig. 2h). Consistent with the XRD results shown in Fig. 1, the 4-variants or single-variant domain configurations are deterministically stabilized by the underneath buffer layer [LSMO(110) or STO(110)]. Given an intermediated buffer layer thickness, the pole figures exhibit a coexistence of both domain configurations (Supplementary Figs. S3 and S4), signifying a mixed HZO(100)$_O$ and HZO(111)$_O$ phases. The distinct epitaxial relationships between the HZO/LSMO/STO(110) and HZO/STO(110) heterostructures can be further corroborated by the 3-dimensional reciprocal space mappings (3D-RSM, See Supplementary Figs. S5 and S6).

Since HZO is polarized along the [001]$_O$ axis[32], FE polarization of multi-domain HZO(111)$_O$ film should consist of both the out-of-plane and in-plane components. By contrast, the single-domain HZO(100)$_O$ film is expected to show uniaxial in-plane polarization. Based on this consideration, we quantitatively compare the FE properties of these

two types of HZO samples. For the HZO(111)$_O$/LSMO/STO(110) sample, the electric field-dependent out-of-plane polarization (P_{out}-E) curves display well-defined FE hysteresis loops, and the piezoresponse force microscopy (PFM) images display strong out-of-plane PFM signal but a weak in-plane PFM signal (Supplementary Figs. S7 and S8), consistent with our previous reports[25,33]. For the 10-nm thick HZO(100)$_O$/STO(110) film, we patterned interdigitated Pt top electrodes to apply lateral E and measured the in-plane polarization (P_{in}) (Fig. 3a, see Methods for details)[34]. The P_{in}-E curves measured along the in-plane HZO[001]$_O$ axis (Fig. 3b) display well-defined FE hysteresis loops and the remnant polarization (P_r) value reaches ~20.6 μC/cm². By contrast, the P_{in}-E loop measured along the in-plane HZO[010]$_O$ axis shows a dramatically reduced P_r below 4.8 μC/cm² (Fig. 3c and Supplementary Fig. S9). Moreover, the P_{out}-E curve measured from the HZO(100)$_O$ film grown on the Nb-doped STO(110) [Nb:STO(110)] substrate displays a negligible FE signal (Fig. 3d). We also measured the P_{in}-E hysteresis loops in the positive-up-negative-down (PUND) mode (Supplementary Figs. S10 and S11) and acquired both the in-plane and out-of-plane PFM images (Supplementary Fig. S12). These results further verified the intrinsic nature of FE polarization switching along the in-plane HZO[001]$_O$ axis.

To further elucidate the uniaxial nature of FE polarization in the HZO/STO(110) sample, we conducted rotational in-plane PFM
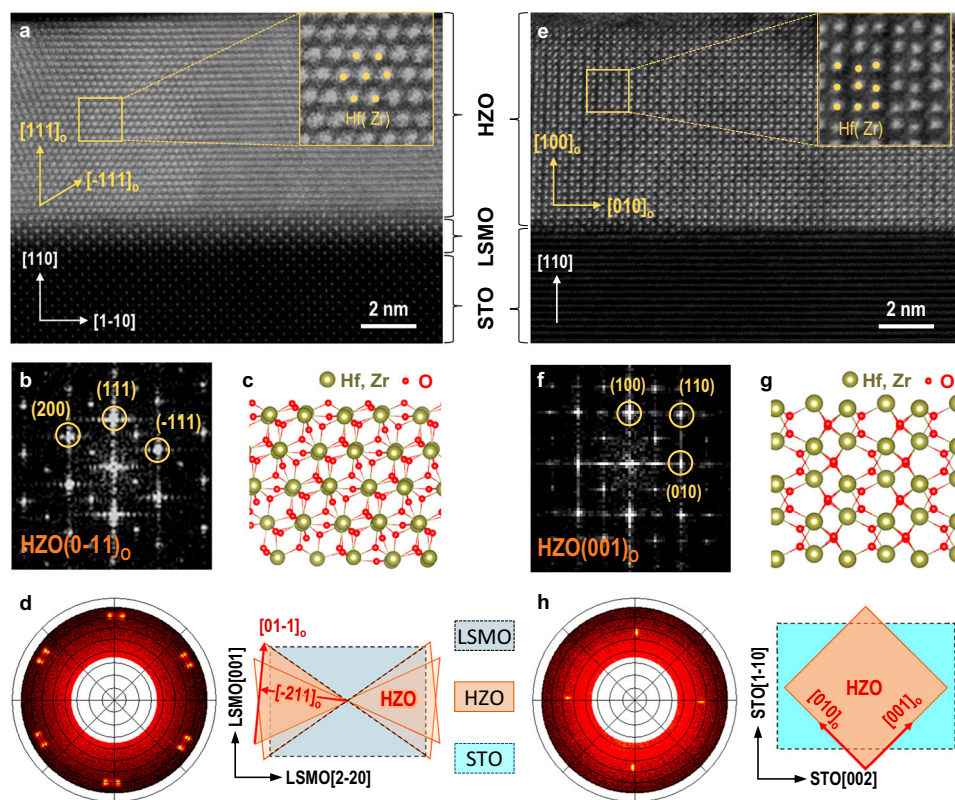
Fig. 2 | Atomic structures, domain configurations, and epitaxial relationships of HZO-based heterostructures. a HAADF-STEM image of the HZO(10 nm)/LSMO(5 u.c.)/STO(110) heterostructure, viewed along the STO[001]$_c$ zone-axis. The inset of (**a**) is a zoom-in STEM image acquired from the area marked in the yellow box. **b** FFT pattern of a (111)$_O$-oriented O-phase HZO domain. **c** Structure model of the O-phase HZO, viewed along [0-11] axis. **d** Left panel: Pole figure measured from the HZO(10 nm)/LSMO(5 u.c.)/STO(110) sample at $2\theta \sim 30.2°$. The φ and χ scanning ranges are 0–360° and 35–80°, respectively. Right panel: Schematic in-plane epitaxial relationships between the HZO(111)$_O$ domains and the underlying LSMO(110)

bottom electrode. **e** HAADF-STEM image of the HZO(10 nm)/STO(110) heterostructure, viewed along the HZO[001]$_O$ axis. The inset displays a zoom-in image acquired from the area marked in the yellow box. **f** FFT pattern of a (100)$_O$-oriented O-phase HZO domain. **g** Structure model of the O-phase HZO, viewed along the HZO[001]$_O$ axis. **h** Left panel: Pole figure about {11-1} peaks measured from the HZO/STO sample at $2\theta \sim 30.2°$, The φ and χ ranges are 0–360° and 35–80°, respectively. Right panel: Schematic in-plane epitaxial relationships between the HZO(100)$_O$ lattice and the STO(110) substrate.

characterizations. During scanning, a biased PFM tip can induce an effective trailing E (E_{trail}) parallel to the slow-scan axis (Fig. 3e)[35]. By applying positive and negative biases on the tip, we poled the in-plane polarized stripe domains on the HZO(100)$_O$ film and then conducted the in-plane PFM measurements. The PFM contrast (Fig. 3f, g) is highly sensitive to the angle between the PFM slow-scan axis and HZO[001]$_O$ axis (θ_{scan}). At $\theta_{scan} = 0°$, the alignment of E_{trail} along the polar axis [001]$_O$ gives rise to a strong PFM contrast. As θ_{scan} increases, both the PFM contrasts decay gradually and become negligible at $\theta_{scan} = 90°$, further confirming the [001]$_O$-oriented in-plane FE polarization. We also measured the P_{in}-E hysteresis loops and in-plane PFM images on the HZO(100)$_O$/STO(110) films with variable t_{HZO} (Supplementary Figs. S13–S16 and Supplementary Table S1). These results suggest that the uniaxial in-plane ferroelectricity persists even when t_{HZO} reduces to 1.0 nm.

In addition to the robust uniaxial in-plane ferroelectricity, the HZO(100)$_O$ film also exhibits a dramatically reduced E_C. Figure 4 summarizes a series of E_C - t_{HZO} curves extracted from the literature[36–43]. For the polycrystalline HZO films, the E_C varied significantly from 1 to 30 MV/cm, probably due to the mixed structural polymorphs and disordered domain configurations[16,20,21,36–39]. For the HZO(111)$_O$/LSMO epitaxial films, the E_C-t_{HZO} curves follow the Janovec-Kay-Dunn law [$E_C \propto (t_{HZO})^{-2/3}$][40,41]. Despite higher ordered out-of-plane domain orientations, E_C values of these epitaxial HZO films are in the range of 2-10 MV/cm[22,23,40–43], still more than one order of magnitude higher than the typical E_C values of perovskite oxide-based

ferroelectrics. The high E_C of HZO is related to its intrinsically higher polarization reversal barrier[16,44]. By contrast, the E_C of the in-plane polarized HZO(100)$_O$ films is nearly one order of magnitude lower than that of the HZO(111)$_O$/LSMO epitaxial films. Especially for the 10 nm and 15 nm thick HZO(100)$_O$ films, the E_C reduces down to 0.53 and 0.45 MV/cm, even comparable with the BaTiO$_3$ epitaxial thin films (~10 nm)[45]. In the uniaxially polarized HZO(100)$_O$ layer, the in-plane FE switching is predominately determined by a fast domain wall propagation process along the HZO[001]$_O$ polar axis. Compared to the nucleation-limited FE switching in out-of-plane polarized HZO(111)$_O$, the E required to drive domain wall propagation is much lower[46,47], thus resulting in the ultralow E_C (see detailed discussions in Supplementary Figs. S17 and S18). Although this low E_C still corresponds to a rather large coercive voltage ($V_C \sim 100$ V) due to the lateral measurement geometry, our results strongly indicate that intrinsic E_C of hafnium oxide-based ferroelectrics can be effectively reduced by enhancing the structural and domain uniformities.

Discussion

Now we turn to explore the origin of interface-stabilized HZO(100)$_O$. We first grew the HZO films on a variety of (110)-oriented (in pseudo-cubic notation) perovskite oxide substrates. According to the XRD results (Supplementary Fig. S19), only the STO(110) and Nb:STO(110) substrates can stabilize the HZO(100)$_O$ single-domain configuration, while the LaAlO$_3$(110) [LAO(110)], NdGaO$_3$(110) [NGO(110), corresponding to NGO(100)$_O$], and GdScO$_3$(110) [GSO(110), corresponding
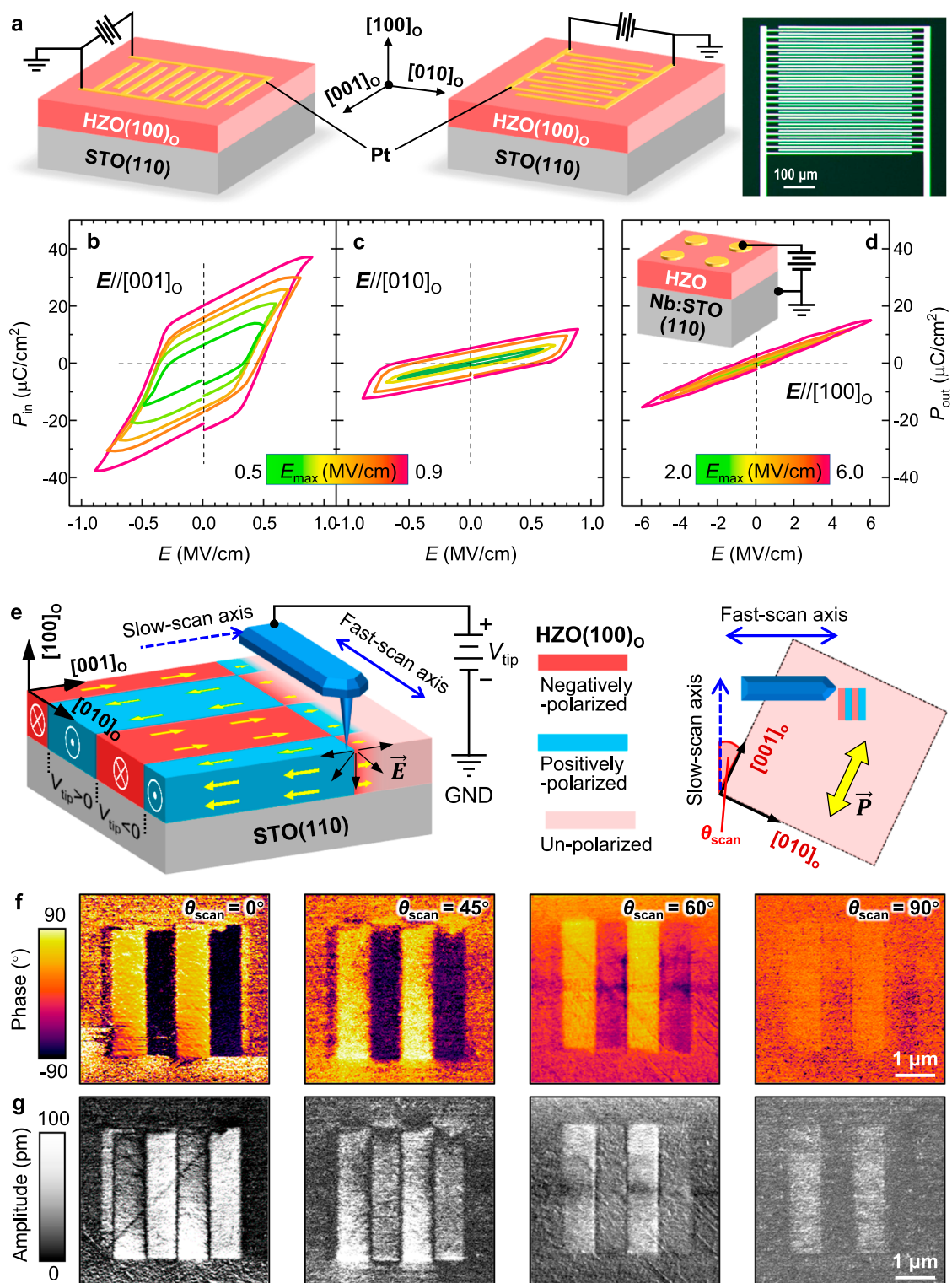
Fig. 3 | Ferroelectric characterizations of HZO/STO(110) films. a Schematic diagram and optical microscopic image of the HZO(10 nm)/STO(110) film with interdigitated Pt electrodes for the in-plane FE characterizations. **b, c** Electric field-dependent in-plane polarization (P_{in}-E) hysteresis loops measured from the HZO(10 nm)/STO(110) film with E//HZO[001]$_O$ (**b**) and E//HZO[010]$_O$ (**c**). The E scanning range (E_{max}) varies from 0.5 to 0.9 MV/cm. **d** E-dependent out-of-plane polarization (P_{out}-E) hysteresis loops measured from the 10 nm thick HZO film grown on Nb:STO(110) substrate. The E scanning range (E_{max}) varies from 2.0 to 6.0 MV/cm. The inset displays the measurement geometry. The top electrodes are circular-shaped Pt pads. **e** Left panel: Schematic diagram of switching the in-plane FE polarization through the tip-induced trailing field. The bias applied on the PFM tip (V_{tip}) is ±7 V. Right panel: Schematic diagram for PFM measurements on uniaxial polarization of HZO(100)$_O$/STO(110) sample. The angle between PFM slow-scan axis and HZO[001]$_O$ axis is defined as θ_{scan}. In-plane PFM phase (**f**) and amplitude (**g**) images with θ_{scan} = 0°, 45°, 60°, and 90°. The scanning area is 4 × 4 μm^2.
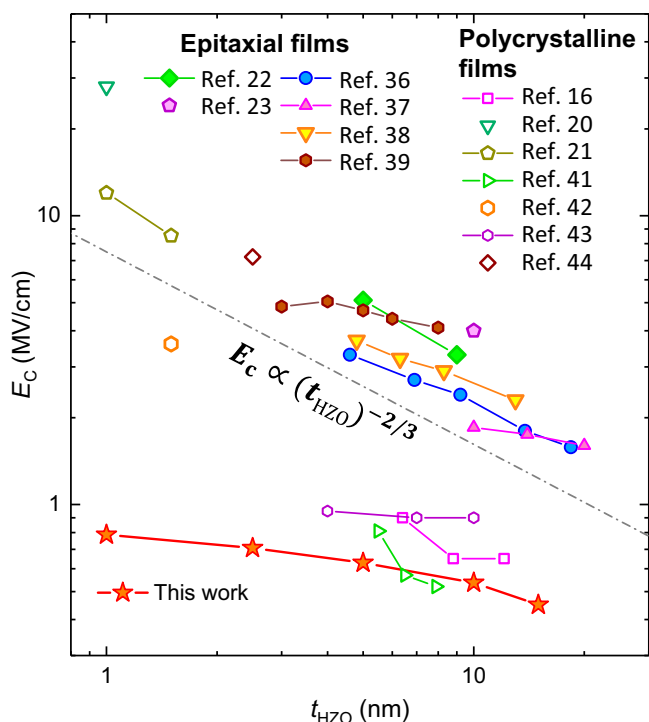
Fig. 4 | Ultra-low coercivity of HZO(100)$_O$/STO(110) films. t_{HZO}-dependent coercive fields (E_C) derived from the HZO(100)$_O$/STO(100) films with various t_{HZO}. A series of t_{HZO}-E_C curves extracted from references are also inserted for comparison. The t_{HZO}-E_C curves of epitaxial (polycrystalline) HZO films are plotted in solid (open) symbols for clarity. The $E_C \propto (t_{HZO})^{-2/3}$ relationship is marked by a dash-dot line.

to GSO(100)$_O$] substrates stabilize the typical HZO(111)$_O$ multi-domain configuration. Considering that these substrates have distinct lattice constants and surface polarities (Supplementary Table S2), we suggest that substrate-imposed epitaxial strain and interfacial polar discontinuity should not be the main driving forces of the observed HZO structure modulation. Since both the insulating STO(110) and semiconductive Nb:STO(110) substrates can stabilize the HZO(100)$_O$ single-domain, we can also rule out the impact of variable interfacial electrostatic screening on the HZO structure. Additionally, we insert a variety of 5 u.c.-thick buffer layers, including NGO, SrRuO$_3$, and La$_{0.67}$Ca$_{0.33}$MnO$_3$ (LCMO) at the HZO/STO(110) interface (Supplementary Fig. S19). None of these buffer layers stabilizes the HZO(100)$_O$ single-domain as STO(110).

According to the above results and discussions, the reorientation of HZO arises from an interface-mediate structure modulation. Hence, the detailed atomic arrangement at HZO(100)$_O$/STO(110) should be reexamined. As shown in Fig. 5a. The high-resolution HAADF-STEM image viewed along the STO[1–10] zone axis displays an atomically-sharp HZO(100)$_O$/STO(110) interface with staggered atomic contrasts (as marked by the yellow line). According to the zoom-in images (Fig. 5b–d), the STEM atomic contrasts gradually transit from Hf(Zr) cation-like to Sr(Ti) cation-like within 1 u.c.-thick interfacial region, signifying a laterally staggered atomic rearrangement in nanoscale (Fig. 5f). Such a unique atomic-scale interfacial reconstruction is absent in the HZO/LSMO interface but recovers at the HZO/STO(5 u.c.)/LSMO interface (Supplementary Figs. S20 and S21). Therefore, the staggered interfacial reconstruction should be unique for the HZO/STO(110) interface, which could be highly correlated to the stabilization of the HZO(100)$_O$ single domain.

During film growth, the surface energy differences between film materials and substrates could be a dominating factor governing the growth mode and crystallographic orientation[48]. Accordingly, we

calculated the surface energies (γ) for various ABO$_3$(110) surfaces and HfO$_2$ (111)$_O$ and (100)$_O$ surfaces (See details in Supplementary Figs. S22, S23, and Supplementary Table S3). As shown in Fig. 5e, both HZO(111)$_O$ and HZO(100)$_O$ surfaces exhibit a rather low γ of 1.12 and 1.14 J/m^2, respectively. These values are close to that of STO(110) ($\gamma = 1.15$ J/m^2). In contrast, other perovskite surfaces show much higher γ values.

Given a much lower γ of HZO than that of the ABO$_3$(110) substrate, domain-matching epitaxy mode should dominate the HZO growth (Fig. 5f), facilitating a preferential growth of HZO(111)$_O$ multi-domains. Specifically, the domain-matching epitaxial mode is divided into two steps. Initially, when 1 or 2 u.c. thick HZO are deposited onto the substrate, the adatoms should weakly bond to the ABO$_3$ surface atoms due to the large difference in γ. As HZO grows thicker, the significant lattice mismatch between HZO and LSMO increases the elastic energy sharply, which then dominates over the interfacial bonding strength. Thus, the HZO tends to grow in an island-like mode with in-plane 4-variants structural domains. This scenario can explain the growth of HZO(111)$_O$ films on LSMO(110), LCMO(110), NGO(110), GSO(110), and LAO(110).

The growth of HZO(100)$_O$/STO(110) film also can be understood based on the mismatches of γ and structural symmetry. The γ values of HZO(100)$_O$ (1.14 J/m^2) and STO(110) (1.15 J/m^2) are relatively low and close to each other, facilitating the formation of interfacial wetting layers[48], i.e. the staggered interfacial layer. Such a nanoscale interfacial reconstruction could effectively accommodate the lattice mismatch between HZO(100)$_O$ and STO(110) and reduce the elastic energy. Thus, the layer-by-layer growth mode persists, leading to the single domain HZO(100)$_O$/STO(110) film. In addition, both the HZO(100)$_O$ and STO(110) share a similar two-fold symmetry, which supports the formation of staggered interfacial reconstruction. Conversely, the HZO(111)$_O$ surface, despite its low γ (1.12 J/m^2), cannot form the interfacial wetting layer with STO(110) due to the large symmetry mismatch. In brief, the single domain HZO(100)$_O$/STO(110) film with uniaxial in-plane FE polarization is stabilized by the synergistic matching in both γ and lattice symmetry.

In summary, by engineering the interfacial atomic structure of ABO$_3$/HZO epitaxial heterostructures, we achieved precise control over the growth orientation and FE polarization direction of HZO films. Unlike the out-of-plane polarized HZO(111)$_O$/LSMO(110) films, the HZO(100)$_O$/STO(110) films exhibit robust uniaxial in-plane ferroelectricity, sustained even at a thickness of 1 nm. Combining both structural characterizations and DFT calculations, we suggest that the HZO(100)$_O$ single domain configuration is stabilized by a synergistic matching in both surface energies and lattice symmetries at the HZO/STO(110) interface. Moreover, the domain wall propagation-dominated in-plane FE switching results in an ultralow E_C of ~0.5 MV/cm. This uniaxially polarized, easily switchable in-plane ferroelectricity offers promising opportunities for designing scalable and energy-efficient in-plane FE tunnel junctions and field-effect transistors, which may contribute to the development of innovative logic and memory devices[11,12]. Furthermore, the perovskite oxide buffer-layer strategy demonstrated here can be extended to manipulate FE polarization and domain configurations in other hafnium oxide-based thin films and heterostructures.

Methods

Sample preparations

We deposited both LSMO and HZO thin films using a custom-built pulsed laser deposition system, equipped with a 248 nm KrF excimer laser. The chamber base pressure is ~10^{-7} Pa, and the sample-to-target distance was fixed at 5.5 cm. For the LSMO layer deposition, the laser fluence, substrate temperature, and oxygen partial pressure were maintained at 2.0 J/cm^2, 700 °C, and 10 Pa, respectively. For the HZO layer deposition, these parameters were set at 1.0 J/cm^2, 900 °C, and
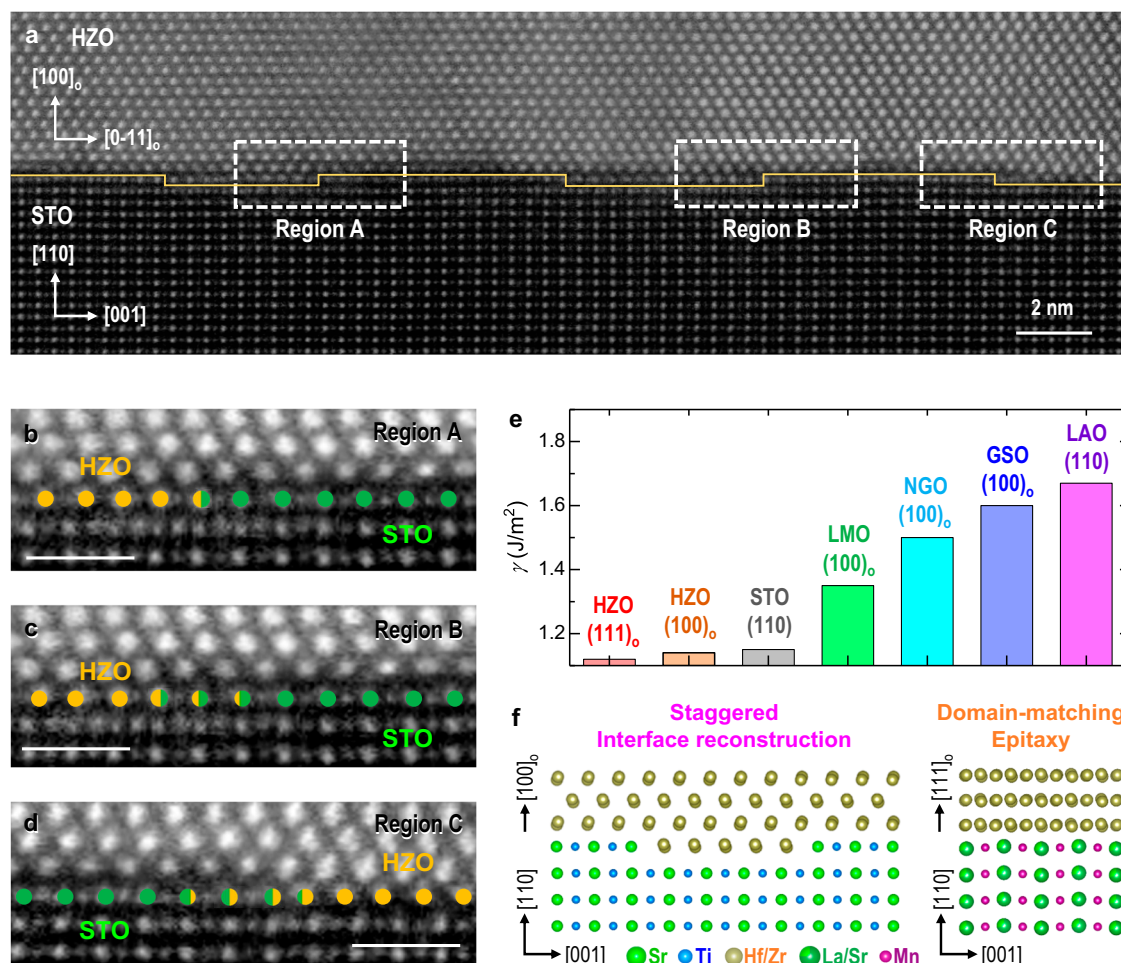
Fig. 5 | Interface reconstruction in the HZO(100)$_O$/STO(110) film. a HAADF-STEM image measured near the HZO/STO(110) interface, viewed along STO[1$\bar{1}$0] zone axis. The solid line (yellow) marks the laterally staggered interface. **b–d** Zoom-in STEM images with HZO/STO step-like atomic contrasts, acquired from 3 pre-selected regions (marked by dashed boxes in (**a**)). The atomic contrasts of Hf(Zr) and Sr are labeled by orange and green circles, respectively. The mixed Hf(Zr) and Sr contrasts are marked by the bi-color circles. **e** DFT-calculated surface energies (γ) of different HZO(111)$_O$, HZO(100)$_O$, and several representative pseudo-cubic (110)-oriented ABO$_3$ surfaces. **f** Schematic atomic structure of HZO(100)$_O$/STO(110) interface with staggered reconstruction and HZO(111)$_O$/LSMO(110) interface with domain-matching epitaxy growth mode.

10 Pa, respectively. After deposition, the heterostructures were sub-sequently in-situ annealed for 15 min and then cooled down to room temperature at 30 °C/min.

Structural characterizations

We characterized the structural properties of the HZO films using XRD and STEM. Crystallographic analyses of the HZO thin films and HZO/LSMO bilayer heterostructures were carried out using a high-resolution X-ray diffractometer (PANalytical Empyrean, Cu Kα1 radiation) in both 2θ-ω linear scan and pole figure modes. During the pole figure measurements, the incident beam was configured in point focus mode, and both the φ angle (in-plane sample rotation angle around the substrate surface normal direction) and χ angle (inclination angle from the substrate surface normal) were scanned in tandem, with the detector fixed at the Bragg angle of targeted reflection. Specifically, φ scans from 0° to 360° at incremental χ angles ranging from 35° to 80°, with 1° intervals. This approach effectively assesses epitaxial relationships and structural domain configurations of the HZO/LMSO/STO(110) and HZO/STO(110) heterostructures.

Additionally, we performed synchrotron-based 3-dimensional XRD reciprocal space mapping at the SSRF BL02U2 beamline with an X-ray energy of 18.27 keV (wavelength of 0.6785 nm). Diffraction data

were collected using a Huber six-circle diffractometer and an EigerX 500 K pixel detector.

STEM specimens were prepared using a Thermo Scientific Helios 5 CX focused ion beam. Before ion-beam milling, an amorphous carbon layer was deposited on the surface of HZO thin films for protection. Cross-sectional lamellae (~100-nm thick) were initially cut from the HZO-based heterostructures using a Ga$^+$ ion beam at an acceleration voltage of 30 kV. These lamellae were subsequently thinned down to about 40 nm using Ga$^+$ ion beams at reduced acceleration voltages of 5 kV and 2 kV. Atomic-resolution HAADF-STEM imaging was conducted using a Thermo Scientific Themis Z microscope operated at 300 kV and equipped with a probe-forming aberration corrector.

Ferroelectric characterizations

Both the P_{out}-E and P_{in}-E loops were measured via a Radiant Precision Premier LC Ferroelectric Tester. During the measurements, triangular voltage pulses with a frequency of 1 kHz were applied, and the maximum magnitude of voltage pulse (V_{max}) was 200 V. For measuring the P_{in}-E loops, platinum (Pt) films were magnetron sputtered onto the HZO/STO(110) film surface and patterned into interdigitated electrodes via photolithography. As shown in Supplementary Fig. S9a, b, we patterned an array of interdigitated electrodes with E parallel to HZO[100]$_O$, HZO[010]$_O$, and HZO[110]$_O$ axes. The alignment of

interdigitated electrodes was confirmed via XRD pole figure measurements and by referencing the [1–10]-oriented edge of the STO(110) substrate. Within each set of interdigitated electrodes, the lateral distance between adjacent Pt stripes (d) was uniformly controlled at 2 μm. According to the finite element simulations on the spatial distribution of E between two in-plane electrodes via COMSOL Multiphysics (Supplementary Fig. S24), the E strength between interdigitated electrodes is rather homogeneous. Therefore, it is reliable to use the nominal $E = V/d$ for determining the E_C from the P_{in}-E loops measured from the HZO/STO(110) films. The surface morphologies and PFM measurements were performed on HZO films at room temperature using an Asylum Research MFP-3D Origin+ microscope (Oxford Instruments). When measuring PFM, the substrate and bottom electrodes were grounded and the bias (V_{tip}) was applied on a conducting tip. During the in-plane PFM measurements, a biased PFM tip can induce an effective trailing field parallel to the slow-scan axis. By applying positive and negative biases on the tip, we poled the in-plane polarized stripe domains on the HZO(100)$_O$ film and then acquired the in-plane PFM signals.

Density functional theory calculations

DFT calculations are carried out using the Vienna ab initio simulation package (VASP) with the projector-augmented wave (PAW) method[49–51] and the Perdew-Burke-Ernzerhof exchange-correlation functional for solid (PBEsol)[52]. The electronic wave functions are expanded in a plane-wave basis set with a cut-off energy of 600 eV. The ABO$_3$(110) surfaces are modeled with slabs consisting of 11 atomic layers, the thickness of which has been tested converged for the surface energy calculations (Supplementary Fig. S22). Noticed that previous studies[53,54] have shown that the O-terminated stoichiometric STO(110) slab has the lowest surface energy, here we focus on this particular termination. The surface energy of HfO$_2$ is calculated based on the high-temperature precursor T phase, with (101)$_T$ and (001)$_T$ surfaces corresponding to (111)$_O$ and (100)$_O$ surfaces, respectively (Supplementary Fig. S23). The Brillouin zones of ABO$_3$(110), HfO$_2$(001)$_T$, and HfO$_2$(101)$_T$ slab models are sampled with Γ-centred (4 × 3 × 1), (6 × 6 × 1), and (6 × 4 × 1) Monkhorst-Pack k-point meshes[55], respectively. All structures are fully optimized until the residual atomic forces are below 0.01 eV/Å.

Data availability

The data that support the findings of this study are available from the corresponding author upon reasonable request.

References

1. Dawber, M., Rabe, K. M. & Scott, J. F. Physics of thin-film ferroelectric oxides. *Rev. Mod. Phys.* **77**, 1083–1130 (2005).
2. Khan, A. I., Keshavarzi, A. & Datta, S. The future of ferroelectric field-effect transistor technology. *Nat. Electron.* **3**, 588–597 (2020).
3. Garcia, V. & Bibes, M. Ferroelectric tunnel junctions for information storage and processing. *Nat. Commun.* **5**, 4289 (2014).
4. Mikolajick, T. et al. Next generation ferroelectric materials for semiconductor process integration and their applications. *J. Appl. Phys.* **129**, 100901 (2021).
5. Chen, Z. et al. Study of strain effect on in-plane polarization in epitaxial BiFeO$_3$ thin films using planar electrodes. *Phys. Rev. B* **86**, 235125 (2012).
6. Matzen, S. et al. Super switching and control of in-plane ferroelectric nanodomains in strained thin films. *Nat. Commun.* **5**, 4415 (2014).
7. Seidel, J. et al. Conduction at domain walls in oxide multiferroics. *Nat. Mater.* **8**, 229–234 (2009).
8. Balke, N. et al. Enhanced electric conductivity at ferroelectric vortex cores in BiFeO$_3$. *Nat. Phys.* **8**, 81–88 (2012).
9. Oh, Y. S., Luo, X., Huang, F. T., Wang, Y. & Cheong, S. W. Experimental demonstration of hybrid improper ferroelectricity and the presence of abundant charged walls in (Ca,Sr)$_3$Ti$_2$O$_7$ crystals. *Nat. Mater.* **14**, 407–413 (2015).
10. Ma, J. et al. Controllable conductive readout in self-assembled, topologically confined ferroelectric domain walls. *Nat. Nanotechnol.* **13**, 947–952 (2018).
11. Shen, H., Liu, J., Chang, K. & Fu, L. In-plane ferroelectric tunnel junction. *Phys. Rev. Appl.* **11**, 024048 (2019).
12. Kwon, K. C. et al. In-plane ferroelectric tin monosulfide and its application in a ferroelectric analog synaptic device. *ACS Nano* **14**, 7628–7638 (2020).
13. Böscke, T. S., Müller, J., Bräuhaus, D., Schröder, U. & Böttger, U. Ferroelectricity in hafnium oxide thin films. *Appl. Phys. Lett.* **99**, 102903 (2011).
14. Park, J. Y. et al. Revival of ferroelectric memories based on emerging fluorite-structured ferroelectrics. *Adv. Mater.* **35**, 2201904 (2023).
15. Schroeder, U., Park, M.H., Mikolajick, T. & Hwang, C. S. The fundamentals and applications of ferroelectric HfO2. *Nat. Rev. Mater.* **7**, 653–669 (2022).
16. Wang, Y. et al. A stable rhombohedral phase in ferroelectric Hf(Zr)$_{1+x}$O$_2$ capacitor with ultralow coercive field. *Science* **381**, 558–563 (2023).
17. Li, Y. C. et al. Domain switching characteristics in Ga-doped HfO$_2$ ferroelectric thin films with low coercive field. *Nano Lett.* **24**, 6585–6591 (2024).
18. Park, M. H., Lee, Y. H., Mikolajick, T., Schroeder, U. & Hwang, C. S. Review and perspective on ferroelectric HfO$_2$-based thin films for memory applications. *MRS Commun.* **8**, 795–808 (2018).
19. Cheema, S. S. et al. Emergent ferroelectricity in subnanometer binary oxide films on Si. *Science* **376**, 648–652 (2022).
20. Jo, S. et al. Negative differential capacitance in ultrathin ferroelectric hafnia. *Nat. Electron.* **6**, 390–397 (2023).
21. Fina, I. & Sánchez, F. Epitaxial ferroelectric HfO$_2$ films: growth, properties, and devices. *ACS Appl. Electron. Mater.* **3**, 1530–1549 (2021).
22. Wei, Y. et al. A rhombohedral ferroelectric phase in epitaxially strained Hf$_{0.5}$Zr$_{0.5}$O$_2$ thin films. *Nat. Mater.* **17**, 1095–1100 (2018).
23. Yun, Y. et al. Intrinsic ferroelectricity in Y-doped HfO$_2$ thin films. *Nat. Mater.* **21**, 903–909 (2022).
24. Estandía, S., Dix, N., Chisholm, M. F., Fina, I. & Sánchez, F. Domain-matching epitaxy of ferroelectric Hf$_{0.5}$Zr$_{0.5}$O$_2$(111) on La$_{2/3}$Sr$_{1/3}$MnO$_3$(001). *Cryst. Growth Des.* **20**, 3801–3806 (2020).
25. Liu, K. et al. Anisotropic strain-mediated symmetry engineering and enhancement of ferroelectricity in Hf$_{0.5}$Zr$_{0.5}$O$_2$/La$_{0.67}$Sr$_{0.33}$MnO$_3$ heterostructures. *Adv. Funct. Mater.* **33**, 2209925 (2022).
26. Estandía, S. et al. Engineering ferroelectric Hf$_{0.5}$Zr$_{0.5}$O$_2$ thin films by epitaxial stress. *ACS Appl. Electron. Mater.* **1**, 1449–1457 (2019).
27. Shi, S. et al. Interface-engineered ferroelectricity of epitaxial Hf$_{0.5}$Zr$_{0.5}$O$_2$ thin films. *Nat. Commun.* **14**, 1780 (2023).
28. Shen, Y. et al. Stabilization of ferroelectric Hf$_{0.5}$Zr$_{0.5}$O$_2$ epitaxial films via monolayer reconstruction driven by valence-dependent interfacial redox reaction and intralayer electron transfer. *Phys. Rev. Mater.* **7**, 114405 (2023).
29. Estandía, S. et al. Insights into the atomic structure of the interface of ferroelectric Hf$_{0.5}$Zr$_{0.5}$O$_2$ grown epitaxially on La$_{2/3}$Sr$_{1/3}$MnO$_3$. *Phys. Rev. Mater.* **5**, 074410 (2021).
30. Park, M. H. et al. Effect of annealing ferroelectric HfO$_2$ thin films: In situ, high temperature X-ray diffraction. *Adv. Electron. Mater.* **4**, 1800091 (2018).
31. Sanna, S. et al. Fabrication and electrochemical properties of epitaxial samarium-doped ceria films on SrTiO$_3$-buffered MgO substrates. *Adv. Funct. Mater.* **19**, 1713–1719 (2009).
32. Huan, T. D., Sharma, V., Rossetti, G. A. & Ramprasad, R. Pathways towards ferroelectricity in hafnia. *Phys. Rev. B* **90**, 064111 (2014).

33. Liu, K. et al. Optimizing the ferroelectric performance of $Hf_{0.5}Zr_{0.5}O_2$ epitaxial film by $La_{0.67}Sr_{0.33}MnO_3$ capping layer. *Adv. Electron. Mater.* **10**, 2400136 (2024).

34. Moalla, R. et al. Large anisotropy of ferroelectric and pyroelectric properties in heteroepitaxial oxide layers. *Sci. Rep.* **8**, 4332 (2018).

35. Crassous, A., Sluka, T., Tagantsev, A. K. & Setter, N. Polarization charge as a reconfigurable quasi-dopant in ferroelectric thin films. *Nat. Nanotechnol.* **10**, 614–618 (2015).

36. Park, M. H. et al. Study on the size effect in $Hf_{0.5}Zr_{0.5}O_2$ films thinner than 8 nm before and after wake-up field cycling. *Appl. Phys. Lett.* **107**, 192907 (2015).

37. Gao, Z. et al. Identification of ferroelectricity in a capacitor with ultra-thin (1.5-nm) $Hf_{0.5}Zr_{0.5}O_2$ film. *IEEE Electron Device Lett.* **42**, 1303–1306 (2021).

38. Huang, F. et al. Enhanced switching reliability of $Hf_{0.5}Zr_{0.5}O_2$ ferroelectric films induced by interface engineering. *ACS Appl. Mater. Interfaces* **15**, 50246–50253 (2023).

39. Chernikova, A. et al. Ultrathin $Hf_{0.5}Zr_{0.5}O_2$ ferroelectric films on Si. *ACS Appl. Mater. Interfaces* **8**, 7232–7237 (2016).

40. Lyu, J., Fina, I., Solanas, R., Fontcuberta, J. & Sanchez, F. Growth window of ferroelectric epitaxial $Hf_{0.5}Zr_{0.5}O_2$ thin films. *ACS Appl. Electron. Mater.* **1**, 220–228 (2019).

41. Song, T. et al. Epitaxial ferroelectric La-doped $Hf_{0.5}Zr_{0.5}O_2$ thin films. *ACS Appl. Electron. Mater.* **2**, 3221–3232 (2020).

42. Mimura, T., Shimizu, T., Uchida, H., Sakata, O. & Funakubo, H. Thickness-dependent crystal structure and electric properties of epitaxial ferroelectric Y_2O_3-HfO_2 films. *Appl. Phys. Lett.* **113**, 102901 (2018).

43. Zhou, C. et al. Enhanced polarization switching characteristics of HfO_2 ultrathin films via acceptor-donor co-doping. *Nat. Commun.* **15**, 2893 (2024).

44. Lee, H. et al. Scale-free ferroelectricity induced by flat phonon bands in HfO_2. *Science* **369**, 1343–1347 (2020).

45. Jo, J. Y., Kim, Y. S., Noh, T. W., Yoon, J. G. & Song, T. K. Coercive fields in ultrathin $BaTiO_3$ capacitors. *Appl. Phys. Lett.* **89**, 232909 (2006).

46. Yang, J. et al. Theoretical lower limit of coercive field in ferroelectric hafnia. *Phys. Rev. X* **15**, 021042 (2025).

47. Seshan, K. *Handbook of thin-film deposition processes and techniques* (Noyes Publication, 2002).

48. Smith, D. L. *Thin-film deposition: principles and practice* (McGraw Hill Professional, 1995).

49. Kresse, G. & Furthmüller, J. Efficient iterative schemes for ab initio total-energy calculations using a plane-wave basis set. *Phys. Rev. B* **54**, 11169–11186 (1996).

50. Blöchl, P. E. Projector augmented-wave method. *Phys. Rev. B* **50**, 17953 (1994).

51. Kresse, G. & Joubert, D. From ultrasoft pseudopotentials to the projector augmented-wave method. *Phys. Rev. B* **59**, 1758 (1999).

52. Perdew, J. P. et al. Restoring the density-gradient expansion for exchange in solids and surfaces. *Phys. Rev. Lett.* **100**, 136406 (2008).

53. Eglitis, R. I. & Vanderbilt, D. First-principles calculations of atomic and electronic structure of $SrTiO_3$ (001) and (011) surfaces. *Phys. Rev. B* **77**, 195408 (2008).

54. Heifets, E., Goddard, W. A., Kotomin, E. A., Eglitis, R. I. & Borstel, G. Ab initio calculations of the $SrTiO_3$(110) polar surface. *Phys. Rev. B* **69**, 035408 (2004).

55. Monkhorst, H. J. & Pack, J. D. Special points for Brillouin-zone integrations. *Phys. Rev. B* **13**, 5188 (1976).

Author contributions

L.W. and W.W. conceived the idea and supervised the project. L.W., K.L., F.J., and W.W. prepared the manuscript. K.L., F.J. and J.F. prepared the samples and performed ferroelectric characterizations with the help of Ku.L., J.L., Jia.L., Q.L., K.D., S.S. and Y.Y. And K.L., E.P., Y.T., Hao.H and Z.L. performed XRD structural characterizations and result analyses. X.Z. and C.M. supervised the STEM measurements and analyzed the data. T.Z. and S.L. provided the DFT calculations. S.D. and H.H. conducted the finite elecment simulations. All authors were involved in the data analyses and manuscript preparation.

Competing interests

The authors declare no competing interests.

Additional information

Supplementary information The online version contains supplementary material available at https://doi.org/10.1038/s41467-025-62610-3.

Correspondence and requests for materials should be addressed to Zhenlin Luo, Chao Ma, Shi Liu, Lingfei Wang or Wenbin Wu.

Peer review information *Nature Communications* thanks Jong Yeog Son and Junghyeon Hwang for their contribution to the peer review of this work. A peer review file is available.

Reprints and permissions information is available at http://www.nature.com/reprints

Publisher's note Springer Nature remains neutral with regard to jurisdictional claims in published maps and institutional affiliations.